nature portfolio

https://doi.org/10.1038/s41563-021-01062-8

Supplementary information

Weyl-mediated helical magnetism in NdAlSi

In the format provided by the authors and unedited

Supplementary information for "Weyl mediated helical magnetism in NdAlSi"

Jonathan Gaudet[1,2,3], Hung-Yu Yang[4], Santu Baidya[5], Baozhu Lu[6], Guangyong Xu[2], Yang Zhao[2,3], Jose A. Rodriguez-Rivera[2,3], Christina M. Hoffmann[7], David E. Graf[8], Darius H. Torchinsky[6], Predrag Nikolić[9,1], David Vanderbilt[5], Fazel Tafti[4], Collin L. Broholm[1,2]

[1]*Department of Physics and Astronomy and Institute for Quantum Matter, The Johns Hopkins University, Baltimore, Maryland 21218, USA*

[2]*NIST Center for Neutron Research, 100 Bureau Drive, National Institute of Standards and Technology, Gaithersburg, MD 20899-6102, USA*

[3]*Department of Materials Science and Engineering, University of Maryland, College Park, Maryland 20742, USA*

[4]*Department of Physics, Boston College, Chestnut Hill, MA 02467, USA*

[5]*Department of Physics and Astronomy, Rutgers University, Piscataway, New Jersey 08854, USA*

[6]*Department of Physics, Temple University, Philadelphia, PA 19122, USA*

[7]*Neutron Scattering Division, Oak Ridge National Laboratory, Oak Ridge, Tennessee 37831, USA*

[8]*National High Magnetic Field Laboratory, Tallahassee, FL 32310, USA*

[9]*Department of Physics and Astronomy, George Mason University, fairfax, VA 22030, USA*

1 Structural Characterization of NdAlSi

We characterized the structure of NdAlSi using powder x-ray diffraction, single crystal neutron diffraction, and Energy-Dispersive X-ray spectroscopy (EDX). The results are summarized in Table. S1. Both neutron diffraction and EDX measurements detected Si and Nd vacancies. The noncentrosymmetric $I4_1md$ (#109) and centrosymmetric $I4_1/amd$ (#141) space groups are indistinguishable with X-ray diffraction, and their contrast in neutron diffraction is small. We thus used second harmonic generation (SHG) measurements to distinguish between these space group. SHG is sensitive to a center of inversion in the unit cell. SHG is negligible in a centrosymmetric space group. The large SHG signal reported in the main text points to the noncentrosymmetric space group $I4_1md$ (#109) and is inconsistent with the centrosymmetric space group $I4_1/amd$ (#141).

The SHG data were fit to functions appropriate to four different experimental configurations: 1) incoming polarization rotating, output polarizer fixed with polarization parallel to the crystalline $[010]$ axis, denoted $I_H(\phi)$; 2) incoming polarization rotating, output polarizer fixed with polarization parallel to the $[10\bar{1}]$ axis, denoted $I_V(\phi)$; 3) incoming polarization rotating, outgoing polarizer rotated by 0° relative to the incoming polarization, denoted $I_{\parallel}(\phi)$; and 4) incoming polarization rotating, outgoing polarizer rotated with polarization axis at 90° relative to the incoming polarization, denoted $I_{\perp}(\phi)$.

In the electric dipole approximation, the mathematical forms of these various responses for

the [101] crystal face in the $I4_1md$ space group (C_4v point group) are given by

$$I_{\parallel}^{eee}(\phi) = \frac{1}{32}\cos^2(\phi)\left[(-2\chi_{xxz}^{eee} - \chi_{zxx}^{eee} + \chi_{zzz}^{eee})\cos(2\phi) + 6\chi_{xxz}^{eee} + 3\chi_{zxx}^{eee} + \chi_{zzz}^{eee}\right]^2 \quad (1)$$

$$I_{\perp}^{eee}(\phi) = \frac{1}{8}\sin^2(\phi)\left[(-2\chi_{xxz}^{eee} + \chi_{zxx}^{eee} + \chi_{zzz}^{eee})\cos^2(\phi) + 2\chi_{zxx}^{eee}\sin^2(\phi)\right]^2 \quad (2)$$

$$I_{H}^{eee}(\phi) = \frac{1}{8}\left[(2\chi_{xxz}^{eee} + \chi_{zxx}^{eee} + \chi_{zzz}^{eee})\cos^2(\phi) + 2\chi_{zxx}^{eee}\sin^2(\phi)\right]^2 \quad (3)$$

$$I_{V}^{eee}(\phi) = 2\left[\chi_{xxz}^{eee}\sin(\phi)\cos(\phi)\right]^2 \quad (4)$$

The data were fit to expressions [1-4] accounting for a rotation of the sample axes relative to the laboratory x-axis. This resulted in excellent fits to the data, as seen in Fig. S1. The SHG susceptibilities extracted from the fits are $\chi_{xxz}^{eee} = -115 \pm 3$ pm/V, $\chi_{zxx}^{eee} = 94 \pm 2$ pm/V, and $\chi_{zzz}^{eee} = 564 \pm 5$ pm/V. The competing space group assignment $I4_1/amd$ (point group D_{4h}) is centrosymmetric and thus should not produce as strong of a SHG response as detected here.

2 Neutron scattering from NdAlSi

We determined the spin polarization of the ferromagnetic (FM) $\mathbf{k} = (0, 0, 0)$ magnetic structure of NdAlSi by acquiring rocking scans at 17 symmetrically non-equivalent $\mathbf{k} = (0, 0, 0)$ Bragg positions covering both the $(h, 0, l)$ and (h, h, l) planes. The nuclear and magnetic contributions to the Bragg diffraction were distinguished by collecting rocking scans within both the paramagnetic phase at 10 K and in the commensurate phase at 1.6 K. The Cooper-Nathans formalism was used to calculate the resolution function of our triple-axis experiments [1] and convert the integrated intensities of rocking scans to fully $\mathbf{Q}$-integrated Bragg intensities. Symmetry analysis reveals three possible irreducible representations (irreps) to describe the $\mathbf{k} = (0, 0, 0)$ magnetic structure below T_{c1} [2]: Γ_1

and Γ_3 that respectively correspond to ferromagnetic and antiferromagnetic structures where the spins are oriented along the c axis, and Γ_5 that describes structures where the spins lie in the ab plane. The real parts of the basis vectors associated to each irrep are shown in Fig. S2A. Generally, the $\mathbf{k} = (0, 0, 0)$ spin structure can be described as any linear combinations of all the basis vectors within the three irreps. However, as discussed in the main text, Γ_3 and Γ_5 respectively produce magnetic Bragg reflections at $\mathbf{Q} = (1, 1, 0)$ and $\mathbf{Q} = (0, 0, l)$ positions that were not observed in our diffraction experiments. We used the Nd^{3+} f-electron form factor to refine the magnetic structure of NdAlSi [3]. The final refinement of the neutron diffraction data is plotted in Fig. S3A and it corresponds to the Γ_1 structure with $\mu_{FM} = 1.1(2)\mu_B$. We note that we also collected 10 rocking scans at positions corresponding to the $\mathbf{k} = (3\delta, 3\delta, 0)$ component of the incommensurate spin structure of NdAlSi, and we found that the structure factor of this component matches that of the commensurate $\mathbf{k} = (0, 0, 0)$ component.

We also determined the spin polarization of the antiferromagnetic (AFM) components of the spin structure in both the commensurate ($\delta = 0$) and incommensurate phases ($\delta \neq 0$). To do so, rocking scans at 46 symmetrically nonequivalent Bragg positions were collected within the manifold of Bragg peaks $\mathbf{Q}_+ = \mathbf{G} \pm (\frac{1}{3} + \delta, \frac{1}{3} + \delta, 0)$ and $\mathbf{Q}_- = \mathbf{G} \pm (\frac{2}{3} + \delta, \frac{2}{3} + \delta, 0)$ for both $T = 1.6$ K and 6 K. Here $\mathbf{G}$ refers to all nuclear allowed Bragg peaks. The symmetry analysis of the commensurate $\delta = 0$ phase reveals six possible basis vectors divided into two different irreps (Γ_1 and Γ_2) [2], with real parts as shown in Fig. S2B. The two Nd ions located at $\mathbf{r_1}$=(0,0,0) and $\mathbf{r_2}$=(1/2,0,1/4) in the chemical unit cell have spins anti-parallel to each other for spin structures described by $\vec{\psi}_1$+$\vec{\psi}_2$, $\vec{\psi}_4$-$\vec{\psi}_5$, and $\vec{\psi}_3$. These anti-parallel spin structures lead to strong $\mathbf{Q}_-$ peaks

and no intensity at $\mathbf{Q}_+$ peaks. On the other hand, spin structures described by $\vec{\psi}_1$-$\vec{\psi}_2$, $\vec{\psi}_4$+$\vec{\psi}_5$, or $\vec{\psi}_6$ have parallel Nd spins at $\mathbf{r_1}$ and $\mathbf{r_2}$. This situation leads to strong $\mathbf{Q}_+$ peaks and no intensity at $\mathbf{Q}_-$ peaks. As seen in Fig. S3B, we observed intensities at $\mathbf{Q}_-$ positions that are two order of magnitude greater than at $\mathbf{Q}_+$ so the spin structure is predominantly of the anti-parallel variety. However, since we do detect weak intensity at $\mathbf{Q}_-$ positions there is also a weak common mode spin component for sites $\mathbf{r_1}$ and $\mathbf{r_2}$, which originates from an in-plane spin component μ_{xy}. The reduced mean squared deviation between model and data χ^2 is shown as a function of in-plane component μ_{xy} and its direction θ relative to [110] in Fig. S3C. The minimum χ^2 arises for θ=90°, which is the direction transverse to the ordering vector. The final refinement is shown in Fig. S3A where the best solution was obtained with $\vec{\psi}_1$=-$\vec{\psi}_2$ = 0.14(2)μ_B and $\vec{\psi}_3$=3.8(4)μ_B. Finally, the relative intensities of the $\mathbf{k} = (\frac{2}{3}+\delta, \frac{2}{3}+\delta, 0)$ and $\mathbf{k} = (\frac{1}{3}+\delta, \frac{1}{3}+\delta, 0)$ Bragg peaks within the incommensurate phase are indistinguishable from those of the Ising-like commensurate phase so no spin reorientation was observed above T_{inc}. As seen in Fig. S3D, the χ^2 refinement of the in-plane component within the incommensurate phase is similar to the one obtained for the commensurate phase.

For the AFM component, the spatial variation of the Nd moments is expressed as:

$$\mu_{AFM}(\mathbf{r}) = 1.9(2)(\exp\left(i[(\frac{2}{3}\frac{2}{3}0)\cdot\mathbf{r}+\theta]\right)+\exp\left(-i[(\frac{2}{3}\frac{2}{3}0)\cdot\mathbf{r}+i\theta]\right)). \quad (5)$$

This expression includes both the $\mathbf{k} = (\frac{2}{3}, \frac{2}{3}, 0)$, and $\mathbf{k} = (\bar{\frac{2}{3}}, \bar{\frac{2}{3}}, 0)$ components as required for the magnetic moment to be real for all $\mathbf{r}$. While the diffraction pattern is independent of θ, the real space spin structure does depend on θ. For $\theta = \pi$ the spin structure can be described as (0-up-down) where 0 means there is no net magnetization on this site, whereas a $\theta = 0$ phase shift leads to an (up-down-down) spin structure. Within the commensurate phase, once the FM

component of the structure is added (μ_{FM} = 1.1(2)μ_B), $\theta = 0(4)^\circ$ is the only phase that allows for all the Nd moments to not exceed the 2.9(1)μ_B saturated moment determined by the magnetization data. The intensities of the $\mathbf{k} = (\frac{2}{3}+\delta, \frac{2}{3}+\delta, 0)$ Bragg peaks increase above T_{inc}. A phase shift of $\theta = 12(5)^\circ$ for the $(\frac{2}{3}, \frac{2}{3}, 0)$ and $(\frac{1}{3}, \frac{1}{3}, 0)$ components is needed to respect the same condition within the incommensurate phase.

3 Electronic band structure of NdAlSi

In this section, we present a detailed characterization of the band structure of NdAlSi for the different magnetic phases discussed in the main manuscript. We first analyze the band structure without spin-orbit coupling (SOC) for which the nonmagnetic case is shown in Fig. S4A. For these calculations, the Nd f states were kept in the core. Linear crossings appear along the high-symmetry lines of the first Brillouin zone. The inclusion of ferromagnetism in the calculation, now including the Nd f orbitals in the valence and applying an on-site f Hubbard U of 6 eV, induces a spin-exchange splitting between majority and minority spin channels as shown in Fig. S4B. Just like the nonmagnetic case, multiple linear crossing points appear along the high-symmetry direction. The majority and minority spin channels are colored in blue and red respectively. The majority and minority spin bands have a simple crossing along the $\Gamma - X$ line, while the pattern of crossings is more complex along $S' - Z$, with a tilted crossing very close to the Fermi level, which is in contrast to the nonmagnetic counterpart in Fig. S4A.

We now investigate the band structure of NdAlSi including SOC, starting with the nonmagnetic

band structure shown in Fig. S4C. Because the f orbitals are frozen in the core, they play no role in the active states near the Fermi energy. In this situation, a tiny density of states of $N(E_F) = 0.0012$ states/eV-cell appears at the Fermi level, composed mainly of Nd d, As s and p, and Si s and p orbitals. While there are several type-I linear band crossings near the Fermi level along the high-symmetry lines in the BZ without SOC (Fig. S4A), the presence of SOC in the nonmagnetic calculation causes the linear band crossing points, highlighted by the red boxes in Fig. S4C, to be gapped out along the high-symmetry directions. Instead, Weyl points now appear slightly off the high-symmetry planes in the BZ. The Wannier90 [4] based tight-binding calculation confirms that there are 40 resulting Weyl nodes in the entire BZ, and the locations of the Weyl nodes are plotted in Figs. S4D-E for the top and side views of the BZ, respectively. Four pairs of nodes denoted W_1 are located near the zone-boundary S points, with two pairs near the m_x and two near the m_y mirror planes shown by red dashed lines. Four more pairs named W_2 lie above and below the $k_z = 0$ plane, also near the m_x and m_y planes, but now in the interior of the BZ, shown by dotted lines. Another twelve pairs of Weyl nodes denoted W_3 are arranged around the m_{xy} and $m_{x\bar{y}}$ mirror planes, shown by dashed green lines. The colors of the Weyl nodes reflect their chiralities, with red and blue dots representing nodes with chiralities $+1$ and -1 respectively.

The band structure calculation for the FM phase of NdAlSi including SOC are presented in the main manuscript (Fig. 5). As compared to the nonmagnetic case, the Weyl nodes W_1 near the $k_z = 0$ plane are unaffected by the magnetization along [001], but the nodes lying off the k_z plane along the $S' - Z$ direction undergo further splitting around the m_x and m_y mirror planes. Correspondingly we defined two subtypes: W_2 nodes close to the m_x and m_y mirror planes, and

W'$_2$ nodes away from them. Furthermore, splitting of the W_3 nodes along the m_{xy} and $m_{x\bar{y}}$ mirror planes is observed, which gives rise to new pairs of Weyl nodes categorized into three types: W_3 nodes close to the $k_z = 0$ plane, W'$_3$ off the $k_z = 0$ plane, and W"$_3$ close to the $k_z = 0$ plane but away from the location of the W_3 nodes. To visualize their dispersions, we plot the projected band structure in the vicinity of some representative Weyl nodes in Fig. S5. Figure S5A shows the projected band structure plotted along the k_y direction with the Fermi level coinciding with the Weyl nodes of type W_1 with positive chirality, located 98.6 meV above the charge-neutrality Fermi level. The corresponding two-dimensional Fermi surface projected in the $k_x - k_y$ plane is shown in Fig. S5B. Similarly, the band structure for a Fermi level aligned with Weyl node W_2 is projected along k_y in Fig. S5C, and the same is done for W'$_2$ in Fig. S5E. The Fermi surfaces projected in the $k_x - k_y$ plane at these energy positions are shown in Fig. S5D and F respectively. The cyan-colored circles indicate the Weyl node positions for which the band structures are plotted. The band structure in Fig. S5E, around the W'$_2$ nodes, appear to be of type II (hole and electron pocket touch each other at the node). The Weyl node W_2 in Fig. S5C is at 9 meV and W'$_2$ in Fig. E is at 72 meV above the charge-neutrality Fermi level. Finally, the band structures with Fermi level at the energy positions of the W_3, W'$_3$ and W"$_3$ nodes are shown in Fig. S5G, I and K respectively with the corresponding Fermi surfaces projected in the $k_x - k_y$ plane shown in Fig. S5H, J and L. The W_3, W'$_3$ and W"$_3$ nodes are at 41 meV, 25 meV, and 48 meV above the charge-neutrality Fermi level, respectively.

The computed band structure for the commensurate AFM d-u-u phase of NdAlSi (including SOC) is shown in Fig. S4F, from which 54 Weyl nodes are predicted. The electronic state appears

to have a semimetallic character whose details are extremely sensitive to the structural parameters of NdAlSi, which we know from our neutron diffraction experiment is further complicated by the presence of Si and Nd vacancies on the order of a few $\%$ (Table. S1). Thus, a robust characterization of the Weyl nodes in the d-u-u phase requires further analysis that is beyond the scope of the present manuscript.

4 Quantum Oscillations, Determination of E_F, and nesting vector in NdAlSi

In the main text, we have determined the Fermi surface of NdAlSi in its ferromagnetic phase by comparing the quantum oscillations (QOs) observed in our high-field resistivity measurements wih DFT. Fig. S6A shows the resistivity of NdAlSi measured up to 35 T, where QOs are apparent at high fields. A smooth background was fitted to the data for fields above the metamagnetic (MM) transition, which is marked by a jump in resistivity. To isolate the QOs, we subtracted a smooth background for each temperature. The resulting resistivity data are shown in Fig. S6B. These data show that the $\Delta R = 0$ axis passes through the center of the oscillations, and a monotonic decrease of the oscillatory amplitudes at all fields. Both observations justify our choice of the smooth background.

Next, we performed a fast Fourier transformation (FFT) of the data in Fig. S6B. The resulting FFT spectrum is plotted in Fig. S6C. Based on this spectrum, three distinct frequencies Σ, β, and γ are identified, together with the second harmonic of the β frequency (2β). Note that the β frequency shifts downward as the temperature increases, which agrees with the data presented in the main

text (Fig. 4C). We also determined the effective masses for the three Fermi pockets associated with the QOs peak at Σ, β, and γ. To do this, we fit the standard Lifshitz-Kosevich (LK) formula [5,6] to their QOs amplitudes as a function of temperature (Fig. S6D). The frequencies and effective masses extracted from Fig. S6C and D are listed in Table S2.

Having determined the experimental QOs frequencies, we now turn to the theoretical QO frequencies from DFT calculations. We determined E_F by matching the experiment with the theory. Each E_F corresponds to a specific Fermi surface, which generates a set of QO frequencies. We start from the E_F determined by DFT ($E_F^{DFT} = 6.7473\ eV$, the neutrality point), adjust the E_F below and above E_F^{DFT}, compute QO frequencies for different values of E_F until the calculated QO frequencies match with those we observed in the high-field experiment. For E_F being 30 meV and 33 meV above E_F^{DFT}, the QO frequencies comparable to Σ, β and γ are listed in Table S2. As shown in Table S2, both the theoretical frequencies and effective masses are in decent agreement with the experimental values. We thus choose $E_F = E_F^{DFT} + 30(3)$ meV as the appropriate E_F for the FM phase.

5 The imprint of itinerant electrons' chirality on magnetic order

The defining property of Weyl electrons is their chirality – a Weyl electron's spin and momentum are strongly correlated by the spin-orbit coupling. Here we argue that the magnetic order in NdAlSi exhibits features that are uniquely attributable to such spin-momentum correlations. Specifically, it is hard to explain the small tilting of the magnetic moments from the easy axis in NdAlSi

without the Dzyaloshinskii-Moriya (DM) and Kitaev-type RKKY interactions, which both require a chiral bias in the spin currents of itinerant electrons. The crystal fields that generate the easy-axis spin anisotropy, and the Heisenberg RKKY interactions from conventional Fermi surfaces, would by themselves produce a pristine Ising-like magnetic order (a non-chiral spin anisotropy of spin interactions could introduce a competition with the easy axis, but a non-trivial resolution of such a competition would be a qualitatively different kind of magnetic order, e.g. easy-plane).

The theory of RKKY interactions in magnetic Weyl semimetals [7] predicts the existence of specific DM and Kitaev interactions between the local moments $\mathbf{S}_i$ at lattice sites separated by $\mathbf{r}_{ij} = \mathbf{r}_i - \mathbf{r}_j$:

$$\begin{aligned} H_{\rm DM} &= \sum_{ij} f_{\rm DM}(\mathbf{r}_{ij})\, \hat{\mathbf{r}}_{ij}(\mathbf{S}_i \times \mathbf{S}_j) \\ H_{\rm K} &= \sum_{ij} f_{\rm K}(\mathbf{r}_{ij})\, (\mathbf{S}_i\hat{\mathbf{r}}_{ij})(\mathbf{S}_j\hat{\mathbf{r}}_{ij})\ . \end{aligned} \tag{6}$$

The functions $f_{\rm DM}$ and $f_{\rm K}$ decrease algebraically with the distance $|\mathbf{r}_{ij}|$ and implement the sign-changing spatial modulations of the RKKY interaction strength. The modulations are controlled by the wavevector distance $\Delta\mathbf{Q}$ between a pair of Weyl nodes, and also by a momentum cut-off. Both types of interactions have an extended range beyond the nearest-neighbor sites, and correlate the spin $\hat{\mathbf{n}}$ of local moments with their separation direction $\hat{\mathbf{r}}_{ij}$.

We carried out Monte Carlo simulations of a classical-spin NdAlSi model that contains an approximate but faithful representation of the Heisenberg, DM and Kitaev interactions predicted by

this theory. The full simulated model is

$$H = \sum_{ij} f_{\rm H}(\mathbf{r}_{ij})\,\hat{\mathbf{n}}_i\hat{\mathbf{n}}_j + \sum_{ij} f_{\rm K}(\mathbf{r}_{ij})\,(\hat{\mathbf{n}}_i\hat{\mathbf{r}}_{ij})(\hat{\mathbf{n}}_j\hat{\mathbf{r}}_{ij}) + \sum_{ij} f_{\rm DM}(\mathbf{r}_{ij})\,\hat{\mathbf{r}}_{ij}(\hat{\mathbf{n}}_i\times\hat{\mathbf{n}}_j) - K\sum_i(\hat{\mathbf{z}}\hat{\mathbf{n}}_i)\ .$$

K is the single-site spin anisotropy scale, and the modulated functions of $\mathbf{r}_{ij}\to\mathbf{r}=(x,y,z)$ which contain the other couplings are:

$$\begin{aligned}
f_{\rm H}(\mathbf{r}) &= -\left[J_{\rm H0}+J_{\rm HQ}\cos\left(\frac{2\pi x}{3}\right)\cos\left(\frac{2\pi y}{3}\right)\right]\cos\left(\frac{\pi|\mathbf{r}|}{2\rho}\right)\theta(\rho-|\mathbf{r}|)\,\delta_{z,0} - \sum_{\mathbf{R}} J_{{\rm H}c}(|\mathbf{R}|)\,\delta_{\mathbf{r},\mathbf{R}}\\
f_{\rm DM}(\mathbf{r}) &= -\left[J_{\rm DM0}+J_{\rm DMQ}\cos\left(\frac{2\pi x}{3}\right)\cos\left(\frac{2\pi y}{3}\right)\right]\sin\left(\frac{\pi|\mathbf{r}|}{\rho'}\right)\theta(\rho'-|\mathbf{r}|)\,\delta_{z,0} - \sum_{\mathbf{R}} J_{{\rm DM}c}(|\mathbf{R}|)\,\delta_{\mathbf{r},\mathbf{R}}\\
f_{\rm K}(\mathbf{r}) &= -\left[J_{\rm K0}+J_{\rm KQ}\cos\left(\frac{2\pi x}{3}\right)\cos\left(\frac{2\pi y}{3}\right)\right]\sin\left(\frac{\pi|\mathbf{r}|}{\rho'}\right)\theta(\rho'-|\mathbf{r}|)\,\delta_{z,0} - \sum_{\mathbf{R}} J_{{\rm K}c}(|\mathbf{R}|)\,\delta_{\mathbf{r},\mathbf{R}}
\end{aligned}$$

All two-spin interactions within a single ab plane ($z=0$) are parametrized by two couplings, one for a "uniform" component (0) and another for the component (Q) modulated at the inter-node wavevector $\mathbf{Q}$ which we assume to be $\left(\pm\frac{2\pi}{3},\pm\frac{2\pi}{3},0\right)$ for simplicity. The parameters $\rho=3,\rho'=4$ capture the extended range of these interactions. Note that only the Heisenberg interaction (H) is strongest at shortest distances. The couplings between different ab crystal layers are denoted by the index c, and the inter-layer site separations are labeled by $\mathbf{R}$. The model includes the nearest-neighbor Heisenberg couplings up to the fourth adjacent layer, and up to the first adjacent layer for the weaker DM and Kitaev couplings.

The Monte Carlo calculations based on the simplest Metropolis algorithm and lattice sizes with 15^3 and 30^3 sites quickly reveal that the dominant Heisenberg couplings $J_{\rm HQ}\geq J_{\rm H0}>0$ and the anisotropy $K>0$ stabilize the type of magnetic order seen experimentally in NdAlSi. The ferromagnetic inter-layer couplings then become frustrated and the Metropolis algorithm is unable

to find a long-ranged order in the c-axis direction. This frustration should be resolved by the laterally extended-range RKKY interactions which we didn't model at this time. The spins are perfectly aligned with the c axis (z-direction) in the absence of DM and Kitaev interactions.

Turning on the extended-range DM or Kitaev interactions within the ab-planes was found to have no visible effect on the magnetic order. Spin canting away from the c axis is here precluded by the easy-axis anisotropy: the DM interactions would favor a spin "spiral", but resetting this spiral to the easy-axis extinguishes any local gains from the DM interactions and leaves behind only an energy cost of canting. Similarly, the in-plane Kitaev interactions do not produce enough gain by canting against the energy loss through the spin anisotropy. The DM and Kitaev interactions applied on the inter-layer lattice bonds are a different story – they introduce spin canting shown in Fig.S7, helped by the zigzag lattice bond arrangement along the c direction which breaks the inversion symmetry. The inter-layer Kitaev interactions are found to produce canting which is not consistent with the experiment, but the DM interactions with a negative coupling constant cant the spins in a manner consistent with the observed order, Fig.S7B.

Ions	x	y	z	Occ	U_{11}	U_{22}	U_{33}
Nd	0	0	0	0.96(3)	0.0039(1)	0.0028(1)	0.0019(1)
Al	0	0	0.5841(6)	1.0(2)	0.0070(1)	0.0019(1)	0.0002(8)
Si	0	0	0.4182(5)	0.94(3)	0.0029(1)	0.0026(1)	0.0019(1)

Table S1: **Structural parameters of NdAlSi.** The x, y, and z positions of the Nd, Al and Si ions are tabulated with their occupation number (Occ) and their anisotropic displacement parameters (U_{11}, U_{22} and U_{33}). These parameters were obtained from structural refinement of the single crystal neutron diffraction data assuming the $I4_1md$ (#109) space group with $a = b = 4.1972(1)$ Å, and $c = 14.4915(6)$ Å refined at $T = 100K$.

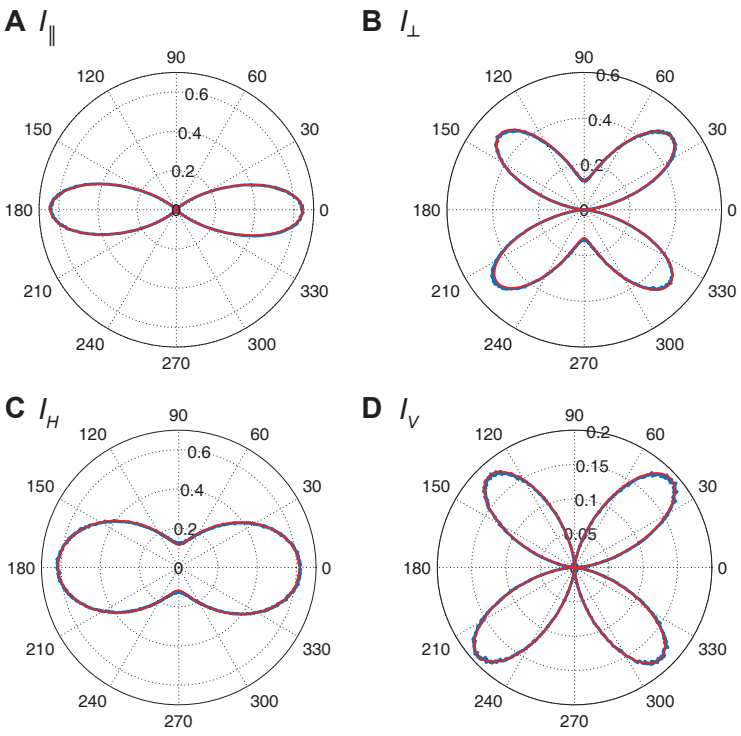

Figure S1: **Second-harmonic generation data in NdAlSi.** The second-harmonic generation (SHG) data for incoming wavelength 1500 nm, outgoing wavelength 750 nm, and fits to bulk electric dipolar SHG in the C_{4v} point group as given by Eqs. [1-4] for (**A**) $I_{\parallel}$, (**B**) $I \perp$, (**C**) I_V, and (**D**) I_H

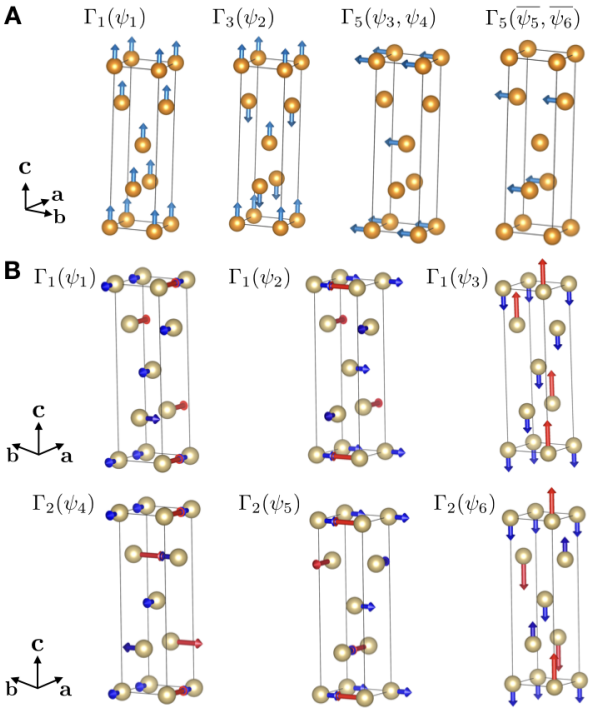

Figure S2: **Symmetry analysis for NdAlSi.** The real parts of the basis vectors for the $\mathbf{k} = (000)$ and $\mathbf{k} = (\frac{2}{3}\frac{2}{3}0)$ spin structures within space group 109 are shown in A and B respectively.

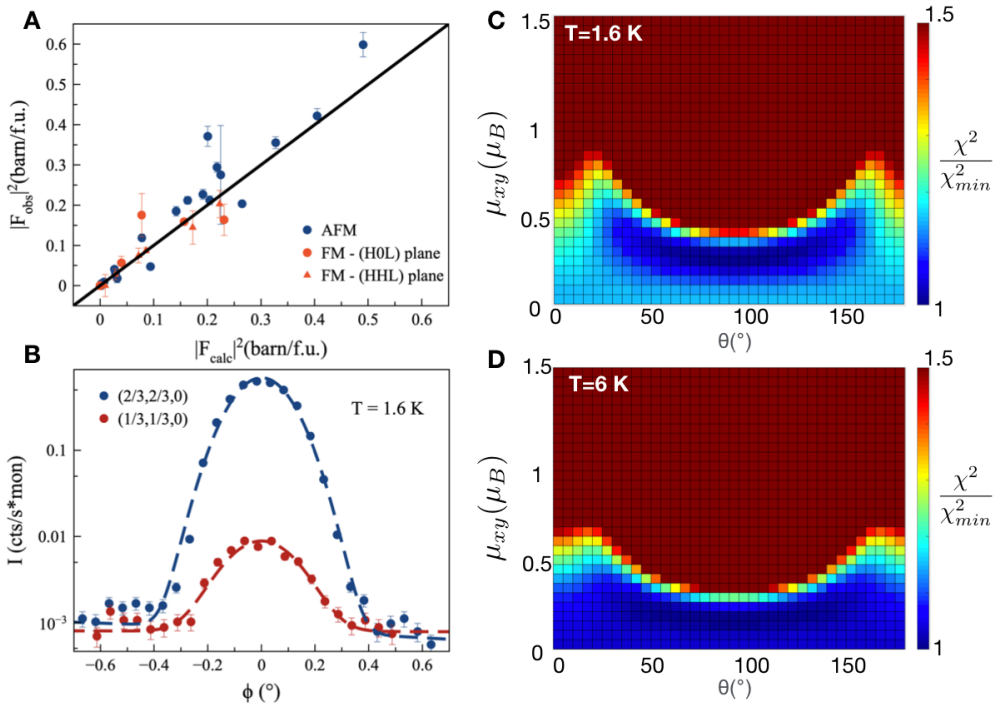

Figure S3: **Magnetic structure refinement of NdAlSi.** The observed magnetic structure factor as a function of the calculated structure factor for both the FM $\mathbf{k} = (000)$ and the AFM $\mathbf{k} = (\frac{2}{3}, \frac{2}{3}, 0)$ components are plotted in A. Low $T = 1.6\ K$ rocking scans at the $\mathbf{Q} = (\frac{2}{3}, \frac{2}{3}, 0)$ and $\mathbf{Q} = (\frac{1}{3}, \frac{1}{3}, 0)$ Bragg positions are compared in B. Note that ϕ is the rocking angle offset from constructive Bragg interference. In C, we plot the χ^2 obtained from refining the commensurate spin structure of NdAlSi as a function of the in-plane component μ_{xy} and its orientation θ relative to [110]. The same map is provided for the incommensurate phase in panel D.

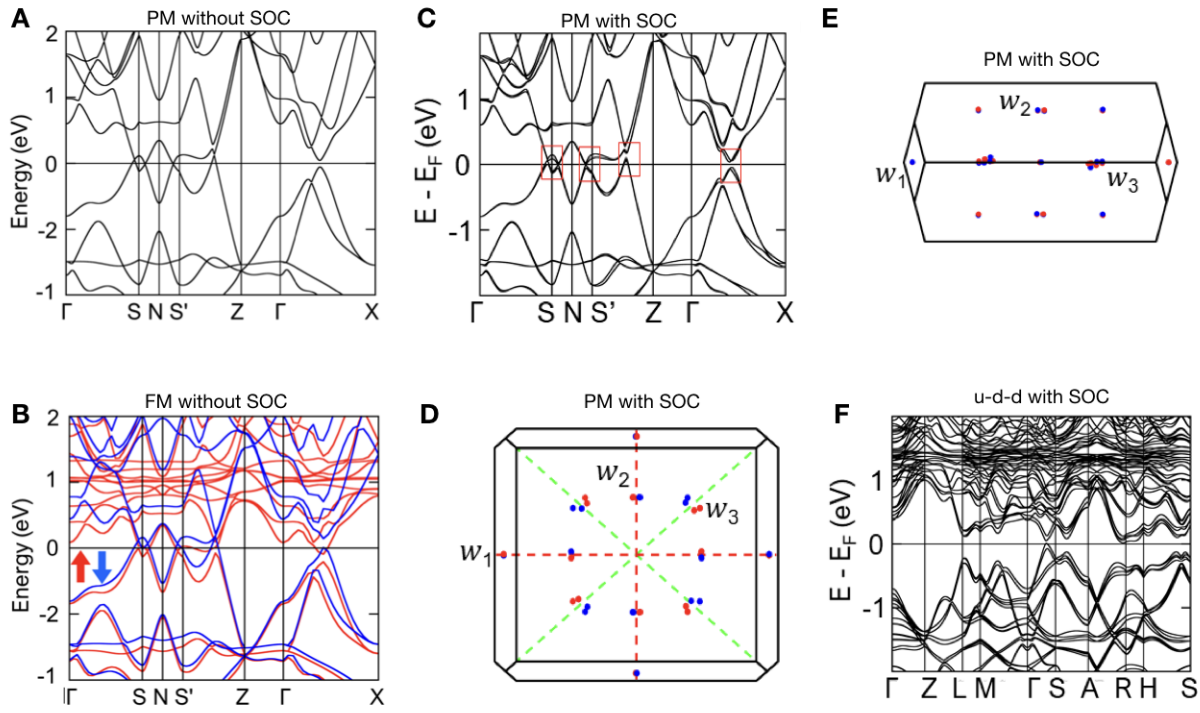

Figure S4: **Band structure of NdAlSi from first-principles calculations.** Paramagnetic state in the PBE approximation, with Nd f states in the core for panel A, and ferromagnetic state in the PBE+U approximation, with Nd f states in the valence for panel B. Panel C is the paramagnetic PBE+SOC band structure where the positions of the Weyl nodes in the first Brillouin zone are shown in panel D and E for this calculation. Three types of Weyl nodes W_1, W_2 and W_3 are marked. The mirror planes are shown by dotted lines. Panel F is the PBE+SOC band structure calculation for the u-d-d phase of NdAlSi.

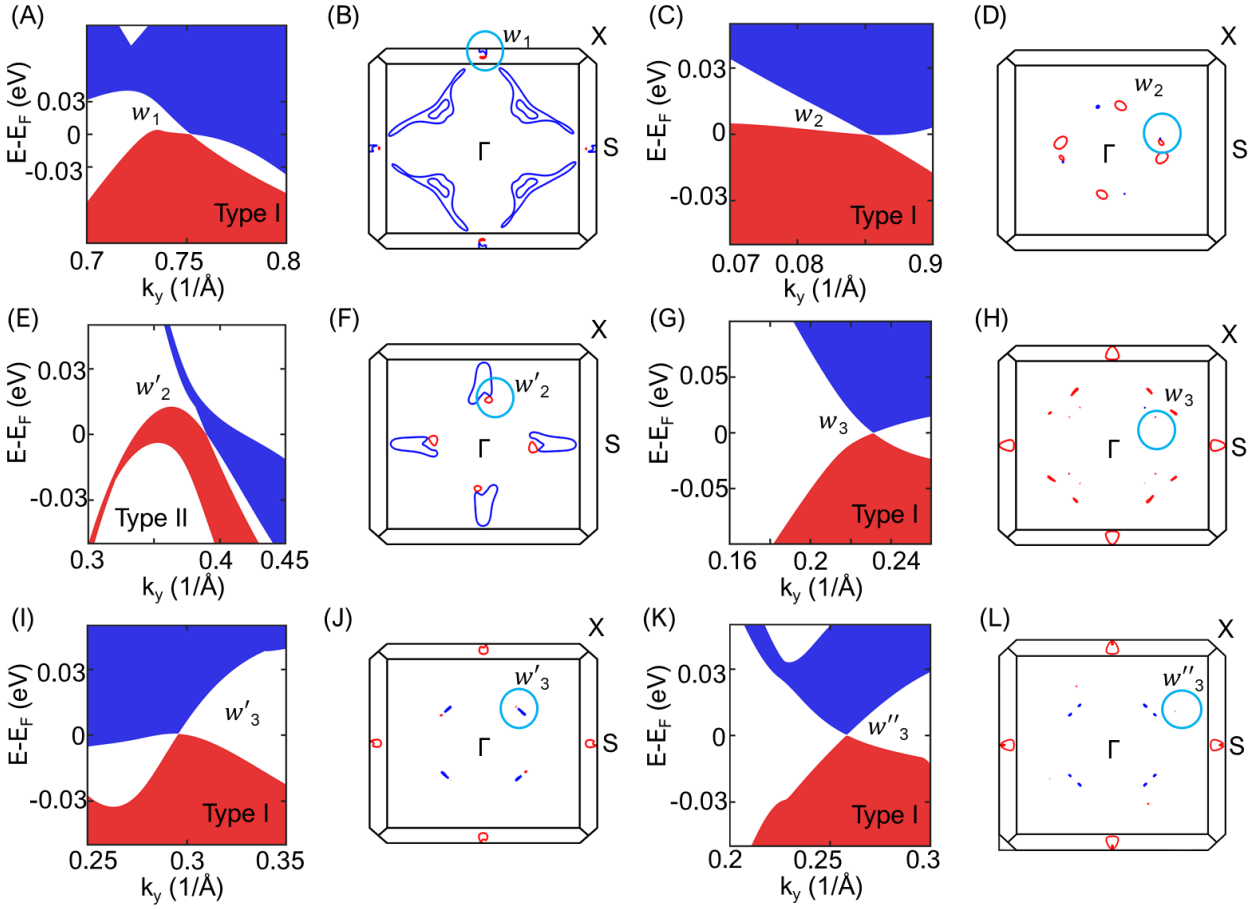

Figure S5: **Band structures, Fermi surfaces, and Weyl node positions as calculated within PBE+U+SOC.** (A-B) Weyl nodes W_1, (C-D) Weyl nodes W_2. (E-F) Weyl nodes W'_2. (G-H) Weyl nodes W_3. (I-J) Weyl nodes W'_3. (K-L) Weyl nodes W''_3.

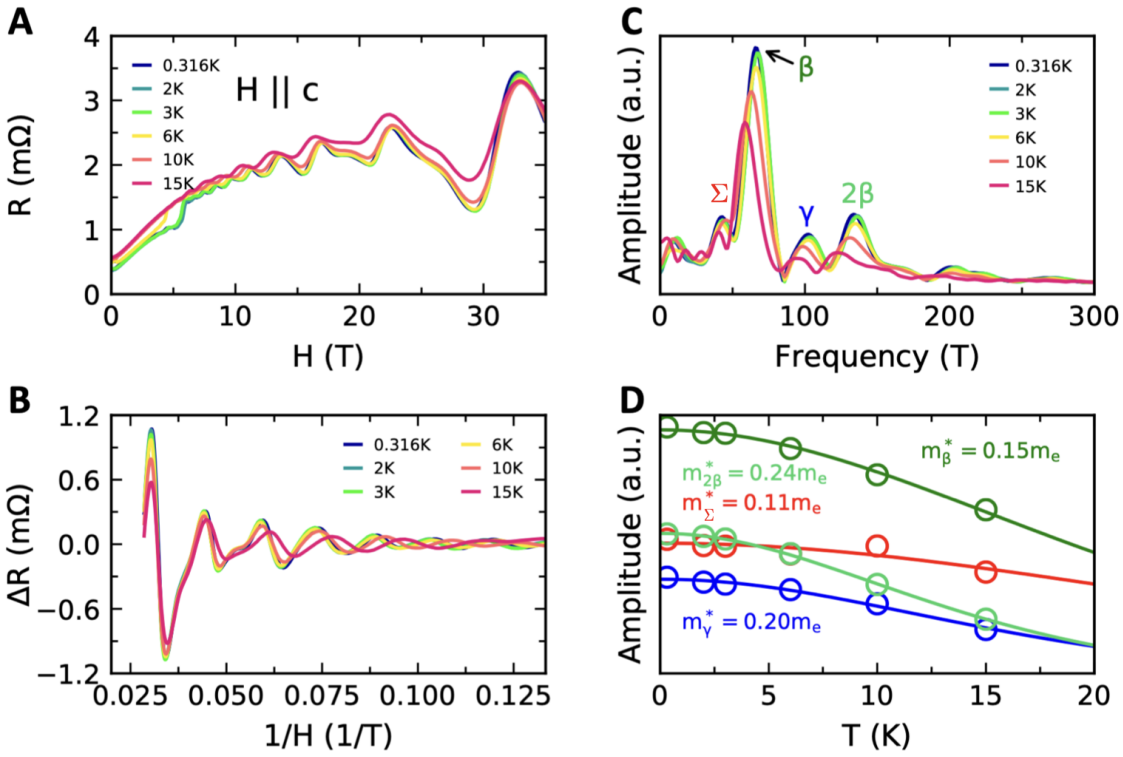

Figure S6: **High-Field Quantum Oscillations in NdAlSi.** Resistivity measured up to 35 T at various temperatures with field along the c-axis in A. Shubnikov–de Haas oscillations appear and grow in amplitude as the field increases. SdH oscillations as a function of $1/H$ at different temperatures in B. The change in the oscillation frequencies can be seen from the shift of peak positions as the temperature increases. The FFT spectrum based on the oscillations in panel B is reported in C. Three distinct Fermi pockets are identified: Σ, β, and γ, and their frequencies at 0.316 K are 40 T, 66 T, and 101 T respectively. The peaks marked by 2β ($F_{2\beta} = 135$ T at 0.316 K) are identified as the second harmonics of β. Note that Σ frequency is different from α frequency ($F_\alpha = 20$ T at $T = 1.8$ K) in the d-u-u phase. The effective masses extracted for each Fermi pocket using a standard Lifshitz-Kosevich formula are reported in D.

Sources	F_Σ (T)	m^*_Σ (m_e)	F_β (T)	m^*_β (m_e)	F_γ (T)	m^*_γ (m_e)
QO	40(5)	0.11(2)	66(5)	0.15(1)	101(5)	0.20(1)
DFT, $+30$ meV	34(1)	0.21(1)	81(1)	0.14(1)	103(4)	0.20(3)
DFT, $+33$ meV	40(1)	0.23(1)	78(1)	0.14(1)	98(4)	0.20(3)

Table S2: **Comparison of Quantum Oscillation (QO) Frequencies.** The frequencies of the Σ, β, and γ pockets derived from resistivity measured up to 35 T, are listed with the results from the DFT calculations. Σ is identified to be an electron pocket, while β and γ are hole pockets. The "+XX meV" in the column "Sources" means the shift in E_F from the DFT-determined E_F for that particular calculation. As a result of such shift, the frequencies change between the calculations "DFT, $+30$ meV" and "DFT, $+33$ meV". The error in E_F is determined to be 3 meV based on the change in E_F from matching F_γ to F_Σ.

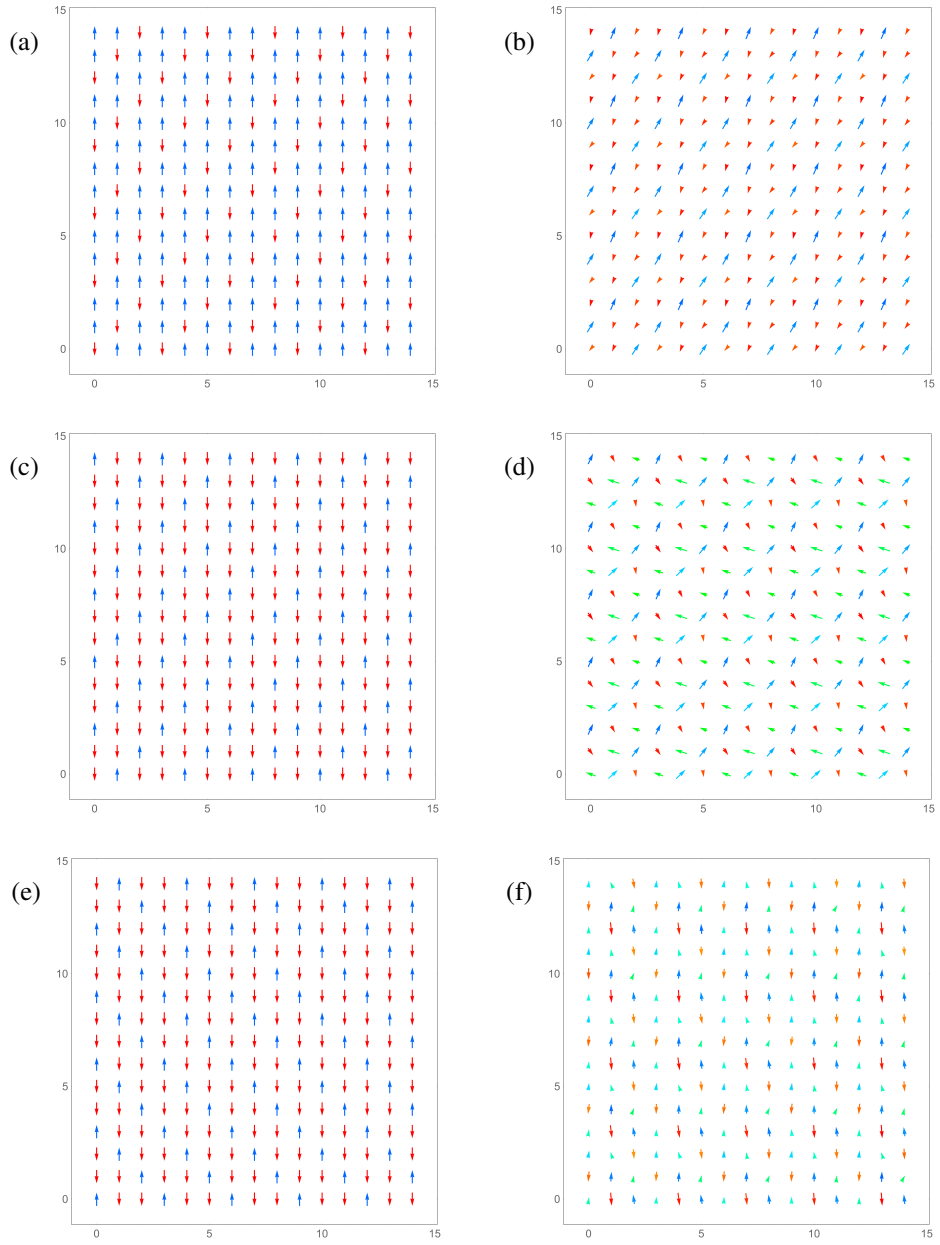

Figure S7: **NdAlSi spin configurations obtained by Monte Carlo.** The left and right columns show the $\hat{\mathbf{z}}S^z$ and $\hat{\mathbf{x}}S^x + \hat{\mathbf{y}}S^y$ components respectively of the local moments on the ab-plane lattice sites (in a layer surrounded by a few other layers with the same magnetic order). The non-zero couplings of the model (7) are $J_{\text{H}0} = 0.4$, $J_{\text{H}Q} = 0.7$, $J_{\text{H}c1} = 0.2$, $K = 1$, and one of the DM or Kitaev couplings on the nearest-neighbor inter-layer bonds: (a-b) $J_{\text{DM}c} = -0.6$, (c-d) $J_{\text{DM}c} = +0.6$, (e-f) $J_{\text{K}c} = 0.6$.

1. Cooper, M.J.T, Nathans, R The resolution function in neutron diffractometry. I. The resolution function of a neutron diffractometer and its application to phonon measurements. *Acta Cryst.* **23(3)**, 357-367 (1967). URL https://doi.org/10.1107/S0365110X67002816.

2. Rodriguez-Carvajal, J. Fullprof. *in satellite meeting on powder diffraction of the XV congress of the IUCr* **127**, (1990).

3. S. W. Lovesey, Theory of neutron scattering from condensed matter Vol 2, *Clarendon Press, Oxford, 1984*

4. Pizzi, G., et al. Wannier90 as a community code: new features and applications. *Journal of Physics: Condensed Matter* **31.16**, 165902 (2020). URL 10.1088/1361-648x/ab51ff.

5. Shoenberg, D. Magnetic oscillations in Metals. *Cambridge University Press*,(2009).

6. Willardson, R. K., Beer, A. C. Semiconductors and Semimetals. *Academic Press* **1**, (1967).

7. Nikolić, P. Dynamics of local magnetic moments induced by itinerant Weyl electrons . *Physical Review B* **103(15)**, 155151 (2021). URL https://link.aps.org/doi/10.1103/PhysRevB.103.155151.